Systematic Design of Coils in Series–Series Inductive Power Transfer for Power Transferability and Efficiency

Ming Lu, *Student Member, IEEE*, and Khai D. T. Ngo, *Fellow, IEEE*

***Abstract*—The quality factor of coils should be high enough to deliver power efficiently during inductive power transfer. To achieve a higher quality factor, coils are designed either with a larger size and thicker wire or with a special structure, making the coils bulky and complicating the fabrication. This paper presents a systematic method to design the coils in series–series inductive power transfer with the smallest possible value of quality factor to realize the requirements of power transferability and efficiency. The electrical parameters of the coils are normalized, decoupled in equations, and designed sequentially. It is found that the smallest value of the quality factor for required efficiency is achieved using an optimal normalized impedance. The physical parameters of the coils are selected sequentially to realize the electrical parameters. This paper presents two operating conditions of series–series inductive power transfer, and example sets of coils with a 100-mm air gap are designed for these operating conditions using the same procedure. The coils were fabricated and tested in a 3.3-kW converter. The measured output voltage (200–400 V for 400 V input) and the coils' efficiency (98.9% at peak power) met the specifications. All switches turned on with zero voltage.**

***Index Terms*—Coil design, inductive power transfer (IPT), normalized parameters.**

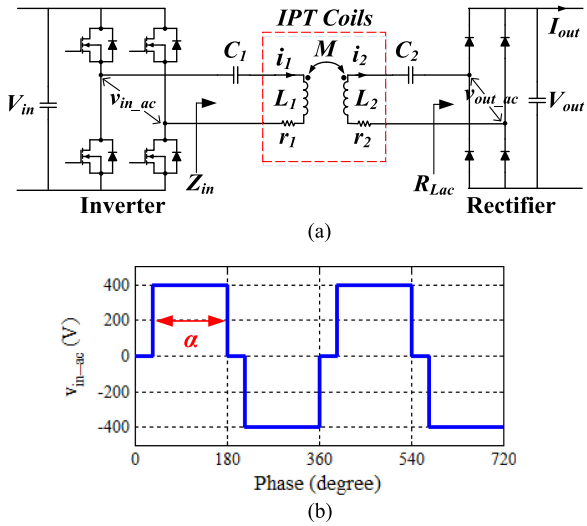

Fig. 1. (a) Circuit topology with series–series compensation of coils for IPT. (b) Output voltage of inverter $v_{\text{in\_ac}}$ with phase shift.

I. Introduction

LOOSELY coupled coils are applied in inductive power transfer (IPT) systems to replace the cables and plugs in conventional charging methods for electric vehicles (EVs) [1]–[4]. Power is transferred through a distance up to tens of centimeters using magnetic resonance and near-field coupling. The advantages of IPT include convenience for drivers, safety when charging in a humid environment, and potential of dynamic charging when vehicles are moving [5], [6].

Compensation for the reactive power needs to be added on both sides of the transmitter and receiver because of the large leakage inductance caused by the air gap. Different compensation topologies have been proposed to improve power transferability and efficiency [7]–[11]. Fig. 1(a) shows a circuit topology with series–series compensation. The switching frequency and inverter output voltage can be tuned for different conditions to realize the desired power transfer [12]–[15]. Coils are crucial to the performance of series–series IPT systems [16]–[20]. The requirements of power transferability and efficiency are satisfied by using the proper design for the coils.

Complex iterations are always required for coils design in IPT [21], [22] because the electrical parameters of coils (e.g., self-inductance, mutual inductance, and winding resistance) and converters (e.g., resonant and switching frequencies, load conditions) are coupled together. Sallan *et al.* [23] demonstrate an iterative process to optimize the coils' power transferability and efficiency using a design factor. Another method by sweeping parameters is proposed in [13] to minimize transmitter current for high efficiency. One way to avoid iterations is to pre-evaluate the coils' performance using the figure of merit (FOM). Waffenschmidt and Staring [24] describe $k*Q$ as the FOM for IPT coils because it determines the maximum efficiency that the coils can potentially achieve when the system operates at resonant frequency under optimal load conditions, where k is the coupling coefficient and Q is the quality factor of the coil. The coils in

Manuscript received January 19, 2017; revised March 21, 2017; accepted April 20, 2017. Date of publication May 19, 2017; date of current version January 3, 2018. This work was supported in part by the High Density Integration Consortium in the Center for Power Electronics Systems and in part by Virginia Polytechnic Institute and State University. Recommended for publication by Associate Editor O. C. Onar. *(Corresponding author: Ming Lu.)*

The authors are with the Center for Power Electronics Systems, the Bradley Department of Electrical and Computer Engineering, Virginia Polytechnic Institute and State University, Blacksburg, VA 24061 USA (e-mail: minglu@vt.edu; kdtn@vt.edu).

Color versions of one or more of the figures in this paper are available online at http://ieeexplore.ieee.org.

Digital Object Identifier 10.1109/TPEL.2017.2706306

[25] and [26] are selected to maximize this FOM. However, in some cases the IPT system does not operate at the resonant frequency, or the load is not optimal for efficiency. It is not intuitive to use $k*Q$ to predict whether the efficiency meets the requirement under specific conditions.

Coils with high Q are preferred in order to meet efficiency requirement. A high Q can be achieved by using coils that either have a larger size and thicker wire, or have a special structure such as that in [27], but these may increase the size and weight of the coils or complicate the fabrication process. In order to minimize the size and ease the fabrication of the coils, the smallest value of Q needed to meet the efficiency requirement should be derived, based on which the coils are designed and fabricated.

The objective of this paper is to systematically design the coils for series–series IPT systems in a sequence to meet given specifications. The requirements of power transferability and efficiency are met using the smallest possible value of Q. Two possible operating conditions of series–series IPTs are discussed: when the compensation capacitor resonates with self-inductance, and when the capacitor resonates with the leakage inductance. When the capacitor resonates with the leakage inductance, there is more circulating energy and its efficiency is lower. Hence, this paper focuses on this case, as it is the most conservative case when designing the coils. However, the design procedure presented here is good for both cases, and it includes two steps: electrical design and physical realization.

The electrical parameters are normalized and then designed sequentially. The normalized parameters include normalized impedance Z_N, coil quality factor Q, normalized switching frequency f_N, coupling coefficient k, and turns ratio n. The power transferability is determined by n. The optimal value for Z_N is selected to meet the efficiency requirement with the smallest possible value of Q. Because all the electrical parameters are normalized, the equations and plots are generalized, and they are applicable for different specifications.

The physical realization of coils is implemented after the electrical design. Planar coils with spiral winding and ferrite plate are usually used for IPTs due to their low profile [28], [29]. Finite-element simulation is used to derive the plots of the electrical parameters (e.g., the coupling coefficient and self-inductance) versus the physical parameters (e.g., inner radii and outer radii of winding). Then the turns number needed to realize optimal Z_N and wire size to satisfy Q are calculated and selected from these plots.

The following section analyzes the IPT with a simplified circuit model and introduces design equations with normalized parameters. Section III presents the procedure to sequentially design electrical parameters for efficient power transfer with the smallest possible Q. Section IV demonstrates the physical realization of coils in a sequence using generalized plots derived from finite-element simulation. In Section V, the coils for a 3.3-kW IPT system with dimensions of 250 mm $\times$ 250 mm and an air gap of 100 mm were built for experimental verification. A loss factor of 1.1% was achieved, and it is close to the desired value for 1%. Section VI concludes this paper. The Appendix provides the details of the procedure used to design coils for the condition when compensation capacitor resonates with self-inductance.

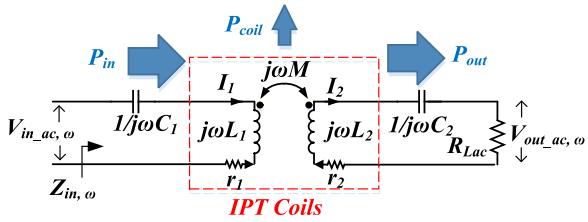

Fig. 2. Equivalent circuit model of the circuit topology in Fig. 1(a).

II. Design Equations for Converter and Coils

Fig. 1(a) shows the circuit topology with series–series compensation of coils for IPT. Resonant frequency f_0 of C_1 and L_1 is the same as that of C_2 and L_2

$$1\Big/\sqrt{L_1C_1} = 1\Big/\sqrt{L_2C_2} = 2\pi f_0 \tag{1}$$

where L_1 and L_2 are self-inductances of transmitter and receiver coils.

The switching frequency and phase-shift between the legs are two commonly used methods to regulate output [12]–[15]. Changing the switching frequency moves the operating point of the system and minimizes the effect when the coupling or load condition changes. The phase-shift controls the inverter output voltage as shown in Fig. 1(b), and it directly regulates the bulk power transferred to the load. Both methods can be used in coordination to control the power transfer and maintain the efficiency.

The simplified circuit model in Fig. 2 is used for analysis. Under the first harmonic approximation, the input dc voltage source and inverter are modeled as sinusoidal voltage source $v_{\text{in\_ac},\omega}(t)$ with peak amplitude $(4/\pi)V_{\text{in}}$, switching angular frequency $\omega_s = 2\pi f_s$, and pulse-width α. The passive rectifier and load are modeled with equivalent resistor $R_{L\text{ac}}$. The expressions of $v_{\text{in\_ac},\omega}(t)$ and $R_{L\text{ac}}$ are

$$v_{\text{in\_ac},\omega}(t) = (4/\pi)\, V_{\text{in}} \sin(\alpha/2) \cdot e^{j\omega_s t} \tag{2}$$

$$R_{\text{Lac}} = \left(8/\pi^2\right) \cdot \left(V_{\text{out}}/I_{\text{out}}\right) \tag{3}$$

where V_{in}, V_{out}, and I_{out} are the input voltage, output voltage, and output current in Fig. 1(a); and α is the pulse-width of inverter output voltage in Fig. 1(b).

Voltage gain M_V in Fig. 2 is defined as the ratio of $V_{\text{out\_ac},\omega}$ over $V_{\text{in\_ac},\omega}$ as in (4). When phase-shift is not used, M_V equals the ratio of V_{out} over V_{in}

$$M_V = |V_{\text{out\_ac},\omega}/V_{\text{in\_ac},\omega}| = V_{\text{out}}/[V_{\text{in}} \sin(\alpha/2)]. \tag{4}$$

The loss factor λ_{coil} of the coils is determined in (5) as the ratio of the coils' loss P_{coil} over the transferred power P_{out} in Fig. 2. The loss factor should be kept small in order to achieve high efficiency.

$$\lambda_{\text{coil}} = P_{\text{coil}}/P_{\text{out}}. \tag{5}$$

When MOSFETS are used in the inverter, high current stress and turn-on loss are caused by reverse-recovery of the body

diode of the opposite switch if zero-voltage turn-on is lost. The inductive impedance in Fig. 2 for soft-turn-ons of the switches, $Z_{\text{in},\omega} = R_{Z\text{in},\omega} + jX_{Z\text{in},\omega}$, is equivalent to positive $\varphi_{Z\text{in}}$. The phase angle of $Z_{\text{in},\omega}$ equals

$$\varphi_{Z\text{in}} = \arctan\left(X_{Z\text{in},\omega}/R_{Z\text{in},\omega}\right). \tag{6}$$

Equations (7) and (8) are derived from Fig. 2 to analyze the behavior of the circuit

$$V_{\text{in\_ac},\omega} = \left[r_1 + j\cdot\left(\omega_s L_1 - 1/\omega_s C_1\right)\right] I_1 - j\cdot\omega_s M\cdot I_2 \tag{7}$$

$$0 = j\cdot\omega_s M\cdot I_1 - \left[r_2 + R_{L\text{ac}} + j\cdot\left(\omega_s L_2 - 1/\omega_s C_2\right)\right] I_2 \tag{8}$$

where L_1 and L_2 are the self-inductances; M is the mutual inductance; r_1 and r_2 are the equivalent series resistances (ESR) of the transmitter and receiver coils at the switching frequency; C_1 and C_2 are resonant capacitors; $R_{L\text{ac}}$ is the equivalent load resistance as in(3); and I_1 and I_2 are the currents of the transmitter and receiver coils, respectively.

The expressions of M_V, λ_{coil}, and $\varphi_{Z\text{in}}$ in (4)–(6) are derived from (7) and (8) [4], [14]

$$M_V = \frac{|j\cdot\omega_s M\cdot R_{L\text{ac}}|}{\left|\begin{array}{c}\left(\omega_s M\right)^2 + r_1\cdot\left(r_2 + R_{L\text{ac}}\right) - \left(\omega_s L_1 - \frac{1}{\omega_s C_1}\right)\left(\omega_s L_2 - \frac{1}{\omega_s C_2}\right)\\ +j\cdot\left[r_1\left(\omega_s L_2 - \frac{1}{\omega_s C_2}\right) + \left(r_2 + R_{L\text{ac}}\right)\left(\omega_s L_1 - \frac{1}{\omega_s C_1}\right)\right]\end{array}\right|} \tag{9}$$

$$\lambda_{\text{coil}} = \frac{r_2}{R_{L\text{ac}}} + \frac{r_1}{R_{L\text{ac}}}\cdot\frac{\left(r_2 + R_{L\text{ac}}\right)^2 + \left(\omega_s L_2 - 1/\omega_s C_2\right)^2}{\left(\omega_s M\right)^2} \tag{10}$$

$$\varphi_{Z\text{in}} = \arctan\frac{\left\{\begin{array}{c}\left(\omega_s L_1 - \frac{1}{\omega_s C_1}\right)\left[\left(r_2 + R_{L\text{ac}}\right)^2 + \left(\omega_s L_2 - \frac{1}{\omega_s C_2}\right)^2\right]\\ -\left(\omega_s M\right)^2\left(\omega_s L_2 - \frac{1}{\omega_s C_2}\right)\end{array}\right\}}{\left\{\begin{array}{c}r_1\left[\left(r_2 + R_{L\text{ac}}\right)^2 + \left(\omega_s L_2 - \frac{1}{\omega_s C_2}\right)^2\right]\\ +\left(\omega_s M\right)^2\left(r_2 + R_{L\text{ac}}\right)\end{array}\right\}}. \tag{11}$$

There are eight unknown parameters in (9)–(11), which are listed in Table I. They are calculated to meet the requirements of power transferability and efficiency. This results in complicated iterations. The parameters in Table I are normalized in Table II in order to simplify the design procedure. The number of unknowns used for calculation is reduced from eight to six.

Coupling coefficient k is used to define the coupling condition of coils in (12). Self-inductances L_1 and L_2 and mutual inductance M are derived from finite-element simulation, or by using the analytical equations presented in [30]–[34].

$$k = M\Big/\sqrt{L_1 L_2}. \tag{12}$$

TABLE I
UNKNOWN PARAMETERS FOR DESIGN OF IPT COILS

Parameters	Symbols
Self-inductance of coil 1	L_1
Self-inductance of coil 2	L_2
Mutual inductance	M
ESR of coil 1 at switching frequency	r_1
ESR of coil 2 at switching frequency	r_2
Load resistance	$R_{L\text{ac}}$
Resonant angular frequency	$\omega_0 = 2\pi f_0$
Switching angular frequency	$\omega_s = 2\pi f_s$

TABLE II
NORMALIZED PARAMETERS FOR DESIGN OF COILS

Parameters	Symbols
Coupling coefficient	k
Normalized switching frequency	$f_N = f_s/f_0$
Normalized impedance of transmitter coil to load	$Z_{N1} = \omega_s L_1/R_{L\text{ac}}$
Quality factor of transmitter coil	$Q_1 = \omega_s L_1/r_1$
Normalized impedance of receiver coil to load	$Z_{N2} = \omega_s L_2/R_{L\text{ac}}$
Quality factor of receiver coil	$Q_2 = \omega_s L_2/r_2$

Using the normalized parameters in Table II, (9)–(11) are represented as (13)–(15):

$$M_V = \sqrt{\frac{Z_{N2}}{Z_{N1}}}\frac{k}{\sqrt{\begin{array}{c}\left[k^2\cdot Z_{N2} + \frac{Q_2 + Z_{N2}}{Q_1\cdot Q_2} - \left(1 - \frac{1}{f_N^2}\right)^2 Z_{N2}\right]^2\\ +\left[\left(1 + \frac{Z_{N2}}{Q_1} + \frac{Z_{N2}}{Q_2}\right)\left(1 - \frac{1}{f_N^2}\right)\right]^2\end{array}}} \tag{13}$$

$$\lambda_{\text{coil}} = \frac{Z_{N2}}{Q_2} + \frac{Z_{N2}}{k^2\cdot Q_1}\left(\frac{1}{Z_{N2}} + \frac{1}{Q_2}\right)^2 + \frac{Z_{N2}}{k^2\cdot Q_1}\left(1 - \frac{1}{f_N^2}\right)^2 \tag{14}$$

$$\varphi_{Z\text{in}} = \arctan\left(1 - \frac{1}{f_N^2}\right)\frac{\left[\left(1 - \frac{1}{f_N^2}\right)^2 - k^2 + \left(\frac{1}{Z_{N2}} + \frac{1}{Q_2}\right)^2\right]\cdot Q_1}{\left[\begin{array}{c}\left(1 - \frac{1}{f_N^2}\right)^2 + k^2\cdot Q_1\cdot\left(\frac{1}{Z_{N2}} + \frac{1}{Q_2}\right)\\ +\left(\frac{1}{Z_{N2}} + \frac{1}{Q_2}\right)^2\end{array}\right]}. \tag{15}$$

To simplify the design, (13) and (15) are replaced with (16) and (17), with the assumption that $Z_{N1} \ll Q_1$ and $Z_{N2} \ll Q_2$. In most cases this assumption is reasonable because the

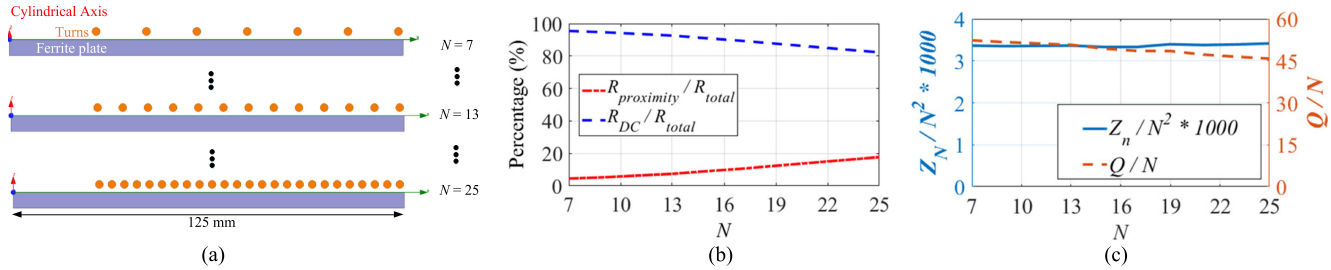

Fig. 3. (a) Cylindrical two-dimensional model of an exemplary coil to analyze influence of proximity resistance. The turns number increases from $N = 7$ to $N = 25$, while the inner radii and outer radii of the winding are kept the same. The litz wire consists of 1650 strands of AWG 44 wires. (b) Percentage of proximity resistance and dc resistance to the total resistance of winding for different values of turns number N at 100 kHz. (c) Normalized impedance Z_N is proportional to N^2 and quality factor Q is proportional to N.

coils' ESR should be small for high efficiency.

$$M_V \approx \sqrt{\frac{Z_{N2}}{Z_{N1}}} \frac{k}{\sqrt{\left[k^2 - \left(1 - \frac{1}{f_N^2}\right)^2\right]^2 Z_{N2}^2 + \left(1 - \frac{1}{f_N^2}\right)^2}} \tag{16}$$

$$\varphi_{Z\text{in}} \approx \arctan\left(1 - \frac{1}{f_N^2}\right) \frac{\left[1 - k^2 \cdot Z_{N2}^2 + \left(1 - \frac{1}{f_N^2}\right)^2 \cdot Z_{N2}^2\right]}{k^2 \cdot Z_{N2}}. \tag{17}$$

When the geometries of the transmitter and receiver coils are the same, L_1 and L_2 are proportional to N^2 where N is the turns number of the litz wire, so Z_{N1} and Z_{N2} are proportional to N^2 as well. The relationship between Q_1, Q_2, and N is more complicated because both dc loss and the proximity effect contribute to the value of Q. The dc resistance is proportional to N because it is related to the length of the coil. The proximity effect is proportional to N^3 because it is proportional to the square of the magnetic field as well as the length of the coil [35]–[37]. However, the proximity effect is weak in the frequency range where IPT works for EV charging. In addition, the coil size for EV applications is large, so usually a limited number of turns are needed, which further weakens the proximity effect. Fig. 3(b) shows the percentages of proximity resistance and dc resistance to the winding resistance versus N for the planar coil shown in Fig. 3(a) at 100 kHz. The proximity effect is not significant. Fig. 3(c) shows that Z_N is proportional to N^2 and Q is roughly proportional to N. Therefore, the relationship between Q_1, Q_2, Z_{N1}, and Z_{N2} is

$$Q_2/Q_1 = \sqrt{Z_{N2}/Z_{N1}} = n \tag{18}$$

where n is the turn ratio of receiver coil over transmitter coil

$$n = N_2/N_1. \tag{19}$$

To simplify the design process, Z_{N1} and Z_{N2} are represented with Z_N as

$$Z_{N1} = Z_N \tag{20}$$

$$Z_{N2} = n^2 \cdot Z_N. \tag{21}$$

Similarly, Q_1 and Q_2 are represented with Q as

$$Q_1 = Q \tag{22}$$

$$Q_2 = n \cdot Q. \tag{23}$$

The equations of M_V, λ_{coil}, and $\varphi_{Z\text{in}}$ in (14), (16), and (17) are simplified using Z_N, Q, and n in (20)–(23) as

$$M_V = n \cdot \frac{k}{\sqrt{\left[k^2 - \left(1 - 1/f_N^2\right)^2\right]^2 \cdot n^4 \cdot Z_N^2 + \left(1 - 1/f_N^2\right)^2}} \tag{24}$$

$$\lambda_{\text{coil}} = n \cdot \frac{Z_N}{Q} + \frac{Z_N}{k^2 \cdot Q} \cdot \left(\frac{1}{n \cdot Z_N} + \frac{1}{Q}\right)^2 + n^2 \cdot \frac{Z_N}{k^2 \cdot Q} \cdot \left(1 - \frac{1}{f_N^2}\right)^2 \tag{25}$$

$$\varphi_{Z\text{in}} = \arctan \frac{\left(1 - 1/f_N^2\right)\left[1 - k^2 \cdot n^4 \cdot Z_N^2 + \left(1 - 1/f_N^2\right)^2 \cdot n^4 \cdot Z_N^2\right]}{k^2 \cdot n^2 \cdot Z_N}. \tag{26}$$

The six unknowns in Table II are now further reduced to five: coupling coefficient k, normalized switching frequency f_N, normalized impedance Z_N, coil quality factor Q, and turns ratio n. The feasibility of sequentially designing these values is demonstrated in next session.

III. Sequential Design of Electrical Parameters

Normalized parameters k, f_N, Z_N, Q, and n are designed for power transferability and efficiency. Fig. 4 shows M_V in (24), $\varphi_{Z\text{in}}$ in (26), and λ_{coil} in (25) versus f_N and Z_N.

The coils are designed for operating conditions when the compensation capacitor resonates with the leakage inductance. Normalized switching frequency f_N equals f_{NH} in this operating condition. The value of f_{NH} is derived from (38) in [38] as

$$f_{\text{NH}} = 1\Big/\sqrt{1-k}. \tag{27}$$

When the switching frequency is no lower than f_{NH}, the highest output voltage is achieved at $f_N = f_{\text{NH}}$. Either using phase-shift or setting $f_N > f_{\text{NH}}$ can realize smaller output

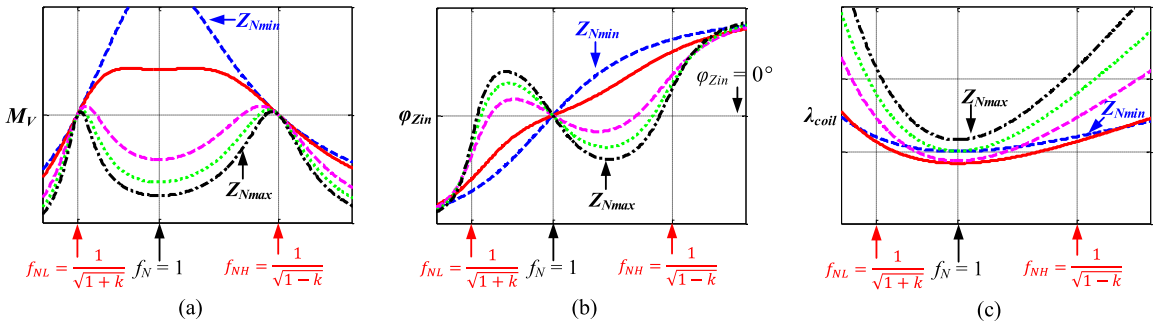

Fig. 4. (a) M_V in (24), (b) $\varphi_{Z\text{in}}$ in (26), and (c) λ_{coil} in (25) versus f_N and Z_N when $n = 1$, $k = 0.25$, and $Q = 1000$.

voltages. The benefits of operating at f_{NH} include easier controllability of output voltage [38], [39] and avoidance of bifurcation when the load conditions change [8], [13], [23]. The major disadvantages to operate at $f_N = f_{\text{NH}}$ include that f_{NH} is dependent on values of k, and λ_{coil} is larger compared to $f_N = 1$, which is shown in Fig. 4(c) and discussed in [40].

The voltage gain M_V in (24), the phase $\varphi_{Z\text{in}}$ of input impedance in (26), and loss factor λ_{coil} in (25) are calculated with $f_N = f_{\text{NH}}$ as

$$M_V = n \tag{28}$$

$$\varphi_{Z\text{in}} = \arctan\left[1/\left(k \cdot n^2 \cdot Z_N\right)\right] \tag{29}$$

$$\lambda_{\text{coil}} = M_V \cdot \frac{Z_N}{Q} + M_V^2 \cdot \frac{Z_N}{Q} + \frac{Z_N}{k^2 \cdot Q}\left(\frac{1}{M_V \cdot Z_N} + \frac{1}{Q}\right)^2. \tag{30}$$

Equation (28) demonstrates that power transferability is realized by simply choosing the appropriate turns ratio n for the coils. Equation (29) shows that $\varphi_{Z\text{in}}$ is always positive when $f_N = f_{\text{NH}}$ for different load conditions.

Ideally, Q should be as high as possible to reduce the loss factor in (30) for high efficiency. This is not practical in many cases because either a special structure of coils or customized thicker wire should be applied to increase Q. It is important to calculate the smallest value of Q that satisfies the efficiency requirement. The loss factor λ_{coil} is determined by Z_N and Q. For each Q, the smallest λ_{coil} is achieved when the partial derivative of (30) to Z_N equals to zero

$$\partial\lambda_{\text{coil}}/\partial Z_N = 0\ . \tag{31}$$

The solution of (31), which is represented as Z_{Nopt}, is derived as

$$Z_{N\text{opt}} = 1\Big/\left(k \cdot M_V \cdot \sqrt{M_V + M_V^2}\right). \tag{32}$$

The smallest value of Q needed to meet efficiency requirements is the case when $Z_N = Z_{\text{Nopt}}$. In (32), Z_{Nopt} is independent of Q and is determined only by k and M_V. This means Z_N and Q can be optimized sequentially. Fig. 5(a) shows Z_{Nopt} versus M_V and k. Because M_V is selected from the specifications, Z_{Nopt} is determined only by k.

The smallest value of Q for the required λ_{coil}, which is represented as $Q_{Z\text{Nopt}}$, is calculated from (30) with k, M_V, and $Z_N = Z_{\text{Nopt}}$. As an example, $Q_{Z\text{Nopt}}$ for $\lambda_{\text{coil}} = 1\%$ is plotted

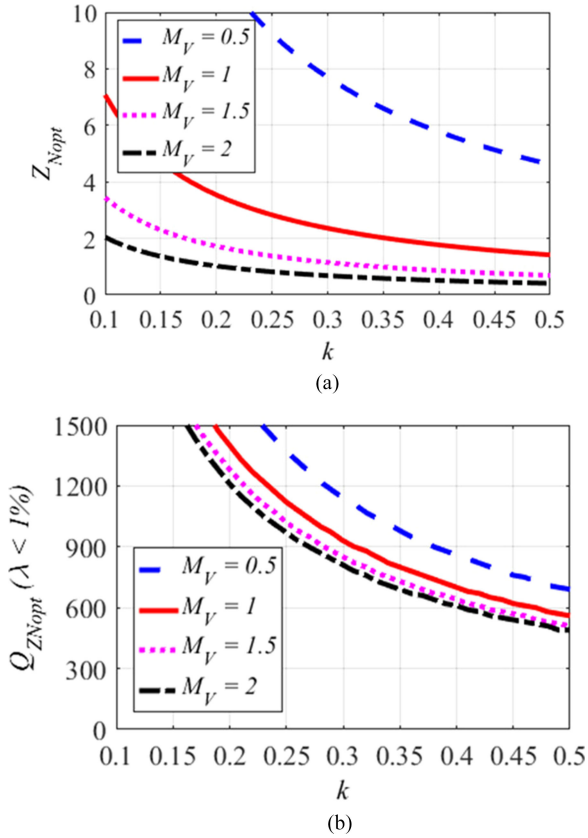

Fig. 5. (a) Z_{Nopt} in (32) and (b) $Q_{Z\text{Nopt}}$ for $\lambda_{\text{coil}} = 1\%$ versus M_V and k when $f_N = f_{\text{NH}}$.

in Fig. 5(b) versus k and M_V. Obtaining a value of $\lambda_{\text{coil}} < 1\%$ is realized with $Q > Q_{Z\text{Nopt}}$. Fig. 5(b) shows that the value of $Q_{Z\text{Nopt}}$ should be larger than 1200 to realize the efficiency requirement when k is lower than 0.2. The size of the coils should be optimized to increase k and to achieve the required λ_{coil} with a practical value of Q. The physical realization of the coils is discussed in detail in Section IV.

Up to now, the normalized parameters n, Z_{Nopt}, and $Q_{Z\text{Nopt}}$ have been derived to meet the requirement of power transferability and efficiency when $f_N = f_{\text{NH}}$ for different values of k. The derived equations and plots in this section are valid for different converter specifications. Table III summarizes the sequential design of electrical parameters. The Appendix provides the detailed procedure used to design the coils when $f_N = 1$.

TABLE III
SEQUENTIAL DESIGN OF ELECTRICAL PARAMETERS

Parameters	Method
n	(28)
$Z_N = Z_{\mathrm{Nopt}}$	(32)
$Q_{Z\mathrm{Nopt}}$ for λ_{coil}	(30)

TABLE IV
SPECIFICATIONS OF IPT COILS FOR DESIGN

Parameters	Method
V_{in} in Fig. 1	400 V
V_{out} in Fig. 1	200–400 V
I_{out} in Fig. 1	8.25 A
f_s	100 kHz
λ_{coil} at peak power	$< 1\%$
Air Gap	100 mm

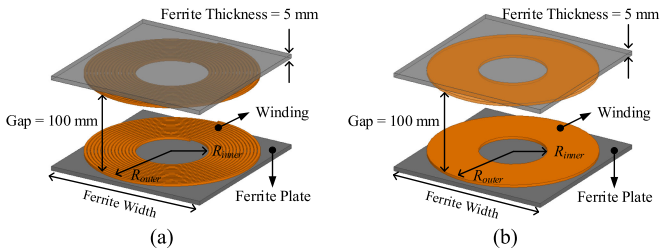

Fig. 6. (a) Structure of planar coils with spiral winding. (b) Simplified coils with single-lumped-turn winding for finite-element simulation.

IV. PHYSICAL REALIZATION OF ELECTRICAL PARAMETERS

Analytical or numerical approaches are usually used for the physical realization of electrical parameters. Analytical equations have been proposed to calculate the inductances of planar coils with air core [30] and infinite-sized ferrite plates [31]–[34]. There is no simple analytical model when it comes to finite-sized ferrite plates. The numerical method is more suitable in this case.

The physical parameters of the coils, such as the inner radii R_{inner} and outer radii R_{outer} of the winding, the number of turns N, and the wire size, are optimized in ANSYS Maxwell [41] to achieve $Z_N = Z_{\mathrm{Nopt}}$ and $Q > Q_{Z\mathrm{Nopt}}$ in Fig. 5. The procedure is demonstrated for the circuit topology in Fig. 1(a) with the specifications in Table IV. The peak value of the output power is 3.3 kW, and the input voltage is 400 V. The output voltage increases from 200 to 400 V, while the output current is to be constant at 8.25 A. The switching frequency is 100 kHz at peak power. Loss factor of the coils λ_{coil} is designed to be less than 1% at peak power.

The ground clearance for EVs is usually larger than 140 mm. The set of coils specified in Table IV is a scaled-down version of the coils that would be used in a real application. The air gap between the transmitter and receiver coils is limited to 100 mm, and the size of the coils is reduced. The scaled-down coils herein are used to verify the design method. The design procedure is the same when the gap between the coils is increased for real applications.

A typical set of planar coils is shown in Fig. 6(a). A circular spiral winding is placed above a square ferrite plate. The circular winding is chosen because of its easy fabrication, and the square ferrite plate is chosen for its easy accessibility with commercial products. This design procedure can also be used for coils with different shapes, as those in [22], [42], and [43]. A single layer of winding is usually used in practice for IPT to control the thickness of the planar coils and the parasitic capacitance.

The physical realization of the coils includes two steps. The first step is sweeping the physical parameters R_{inner} and R_{outer} in finite-element simulation and plotting the electrical parameters k and L versus R_{inner} and R_{outer}. The second step is to sequentially select R_{inner}, R_{outer}, turns number N, and the wire size from the plots to realize the desired electrical parameters for $Z_N = Z_{\mathrm{Nopt}}$ and $Q > Q_{Z\mathrm{Nopt}}$.

A. Parametric Sweep of Physical Parameters

The gap between the coils is 100 mm in this example, as determined by the specifications in Table IV. A 5 mm thick ferrite plate is made of commercialized N95 plates, and the space between the ferrite and winding is set as 1.25 mm. The spiral winding with litz wire shown in Fig. 6(a) is lumped to one flat turn in finite-element simulation with the same R_{inner} and R_{outer}, as depicted in Fig. 6(b). The simulation time is greatly reduced with this simplification, and the accuracy of the simulated inductances and magnetic field using the simplified model in Fig. 6(b) is sufficient for the physical design of the coils [42].

With a 100 mm gap between the coils, R_{outer} and R_{inner} are parametrically swept in finite-element simulation. The ferrite width equals twice R_{outer} in order to achieve the highest k and Q within limited dimensions [20]. The simulated results of coupling coefficient k and one-turn self-inductance L_0 of the simplified model in Fig. 6(b) are plotted in Fig. 7, versus different values of R_{outer} and R_{inner}.

Coupling coefficient k is the same for the coils in Fig. 6(a) and (b). Self-inductance L for coils with N turns of winding in Fig. 6(a) is derived from the self-inductance L_0 of the simplified model with one turn in Fig. 6(b), as

$$L = N^2 L_0. \tag{33}$$

Normalized impedance of the coils in Fig. 6(a) is calculated from the simplified coils in Fig. 6(b) as

$$Z_N = \left(\omega_s N^2 L_0\right) / R_{Lac}. \tag{34}$$

B. Sequential Calculation to Select Physical Parameters

Physical parameters, including inner radii R_{inner}, outer radii R_{outer}, turns number N, and the size of the litz wire, are selected sequentially in this part to realize $Z_N = Z_{\mathrm{Nopt}}$ and $Q > Q_{Z\mathrm{Nopt}}$.

Equation (32) shows Z_{Nopt} is determined by M_V and k. The specifications in Table IV define $M_V = 1$, assuming phase shift is not used for peak power. The values of k for different values of R_{outer} and R_{inner} are plotted in Fig. 7(a). Next the values of Z_{Nopt} for different R_{outer} and R_{inner} are calculated from (32) with $M_V = 1$ and k in Fig. 7(a) and they are plotted in Fig. 8(a).

The turns number N needed to realize $Z_N = Z_{\mathrm{Nopt}}$ is calculated from (34) and plotted in Fig. 8(b). The values of Z_{Nopt}

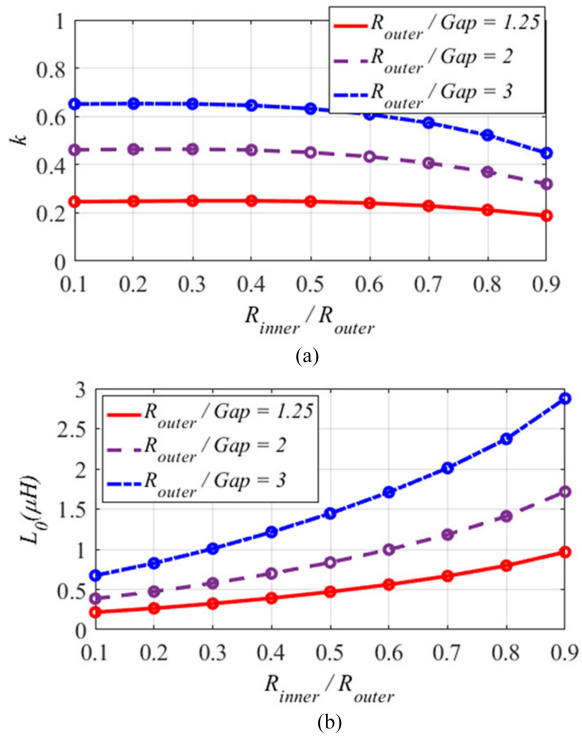

Fig. 7. (a) Coupling coefficient k and (b) self-inductance L_0 of single-lumped-turn model in Fig. 6(b) with gap = 100 mm. The gap is 100 mm as shown in Fig. 6 and Table IV, and $R_{\rm outer}$ is normalized to gap. The normalized $R_{\rm outer} = 1.25$, 2, and 3 represent $R_{\rm outer} = 125$ mm, 250 mm, and 300 mm, respectively.

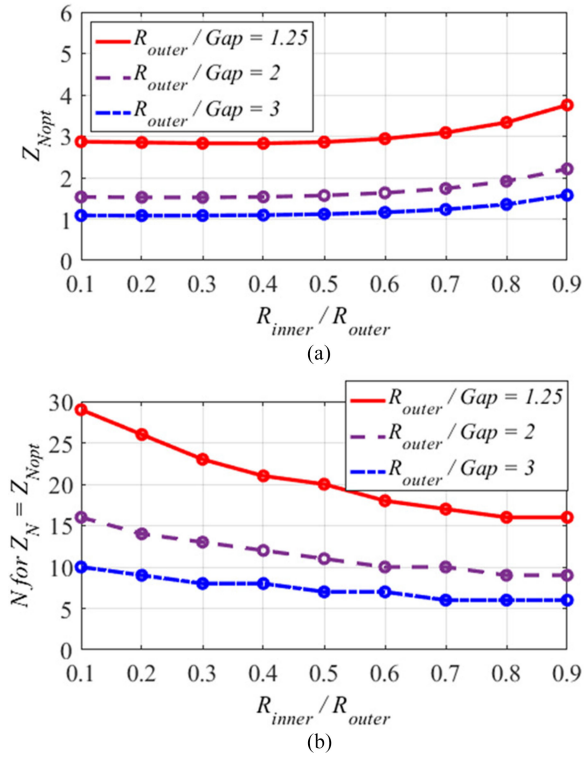

Fig. 8. (a) With simulated k for corresponding $R_{\rm inner}$ and $R_{\rm outer}$ in Fig. 7(a), $Z_{\rm Nopt}$ is calculated from (32) with $f_N = f_{\rm NH}$ and $M_V = 1$. (b) Turns number N to realize $Z_N = Z_{\rm Nopt}$ is calculated from (34) with $Z_{\rm Nopt}$ in (a) and L_0 in Fig. 7(b). The gap is 100 mm as shown in Fig. 6 and Table IV, and $R_{\rm outer}$ is normalized to gap. The normalized $R_{\rm outer} = 1.25$, 2, and 3 represent $R_{\rm outer} = 125$, 250, and 300, respectively.

and L_0 for different values of $R_{\rm outer}$ and $R_{\rm inner}$ are plotted in Fig. 8(a) and Fig. 7(b), respectively. Switching frequency f_s is 100 kHz, and R_{Lac} is 39 Ω at peak power calculated from (3) with $V_{\rm in} = 400$ V and $V_{\rm out} = 400$ V. There are some variations between Z_N calculated from (34) and $Z_{\rm Nopt}$ because N should be an integer, but the variation is small so $Z_N \approx Z_{\rm Nopt}$.

The smallest value of Q needed to satisfy $\lambda_{\rm coil} < 1\%$, which is represented as $Q_{Z\rm Nopt}$, is derived from (30) with $M_V = 1$, k in Fig. 7(a), and $Z_N = Z_{\rm Nopt}$ in Fig. 8(a). The results of $Q_{Z\rm Nopt}$ are plotted for different values of $R_{\rm outer}$ and $R_{\rm inner}$ in Fig. 9(a). This figure shows that the value of $Q_{Z\rm Nopt}$ is smaller for larger coil sizes due to their larger value of k.

Self-inductance L is derived from (33) with L_0 in Fig. 7(b) and N in Fig. 8(b). Mutual inductance M is derived from (12) with k in Fig. 7(a) and L. Inductances are used to calculate or simulate winding currents i_1 and i_2 from Fig. 2. After that, i_1 and i_2 are imported as stranded excitations to the coils in Fig. 6(b) in finite-element simulation. Winding loss $P_{\rm winding}$ is calculated based on the method proposed in [36]. Core loss $P_{\rm core}$ is derived directly from the simulation. The ESR of the coils are determined using

$$r = (P_{\rm winding} + P_{\rm core}) / I^2. \tag{35}$$

The numbers and diameters of strands for the litz wire are swept to guarantee that the value of Q is larger than the value of $Q_{Z\rm Nopt}$ in Fig. 9(a). The diameters of strand are chosen for negligible skin effect at 100 kHz, so strands AWG 40, 42, 44, 46, 48 are taken into consideration. The strands with AWG larger than 48 are not considered because of the cost. The numbers of strands to be swept are selected according to the commercialized products from the manufactures' datasheet. Sullivan [35] describes how to further minimize the winding resistance with the optimal strand number.

Fig. 9(b)–(d) plots the quality factors for litz wires with 660, 1050, 1650, and 2625 strands of AWG 44. The quality factors are calculated from the definition of Q in Table II, with L in (33), $f_s = 100$ kHz, and r in (35). The values of Q using these litz wires are compared with $Q_{Z\rm Nopt}$ for $\lambda_{\rm coil} = 1\%$, with $R_{\rm outer}$ being 125, 200, and 300 mm, respectively. The missing circles for some values of $R_{\rm inner}$ in Fig. 9(b)–(d) mean that the wire is too thick for the number of turns to realize $Z_N = Z_{\rm Nopt}$.

The values of $R_{\rm outer}$ and $R_{\rm inner}$, and the numbers and strands of litz wire that satisfy $Q > Q_{Z\rm Nopt}$ in Fig. 9(b)–(d) are the candidates that meet the requirements for $M_V = 1$ and $\lambda_{\rm coil} < 1\%$ when $f_N = f_{\rm NH}$. The corresponding turns number N is found in Fig. 8(b).

C. Procedure for Physical Realization of Electrical Parameters

Table V summarizes the design procedure and results of the example. Voltage gain M_V is 1 and switching frequency f_s is 100 kHz at peak power according to the specifications in Table IV. The equivalent load resistance R_{Lac} at peak power equals to 39 Ω, calculated from (3) with $V_{\rm in} = 400$ V and $V_{\rm out} = 400$ V.

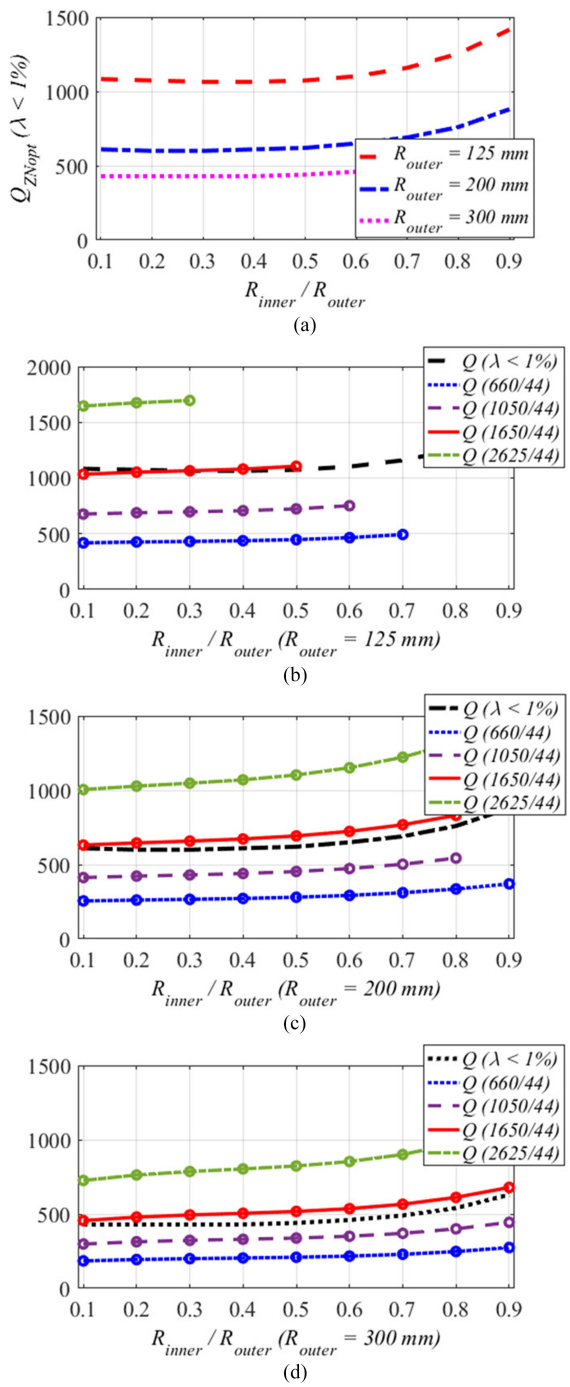

Fig. 9. (a) Q_{ZNopt} calculated from $\lambda_{coil} = 1\%$ in (30) with $Z_N = Z_{Nopt}$ in Fig. 8(a) and k in Fig. 7(a). Q values with different litz wires (660, 1050, 1650, 2625 strands of AWG #44 wire) and turns number N in Fig. 8(b) for R_{outer} of (b) 125, (b) 200 and (b) 300. Candidates for R_{inner} and R_{outer} are to select when $Q > Q_{ZNopt}$.

Outer radii R_{outer}, inner radii R_{inner}, and the number of strands in the litz wire are selected to guarantee $Q > Q_{ZNopt}$ according to Fig. 9(b)–(d). The corresponding k is known from Fig. 7(a). Optimal normalized impedance Z_{Nopt} is calculated from (32) with k and $M_V = 1$. Turns number N for $Z_N = Z_{Nopt}$ is calculated using (34) with the value of Z_{Nopt} in Fig. 8(a) and the value of L_0 in Fig. 7(b).

TABLE V
PROCEDURE OF PHYSICAL REALIZATION AND DESIGN RESULTS ($f_N = f_{NH}$)

Parameters	Design Methods	Values
R_{outer}	$Q > Q_{ZNopt}$ in Fig. 9 ($Q = 1043$)	125 mm
R_{inner}	$Q > Q_{ZNopt}$ in Fig. 9	62.5 mm
Strands number	$Q > Q_{ZNopt}$ in Fig. 9	1650
k	Fig. 7(a) at $R_{inner} = 62.5$ mm and $R_{outer} = 125$ mm	0.247
Z_{Nopt}	(32) with $k = 0.247$ and $M_V = 1$	2.8
N	(34) with $Z_{Nopt} = 2.8$ and L_0 in Fig. 7(b)	20
λ_{coil}	(30) with $Z_N = 2.8$, $Q = 1043$, $k = 0.247$, $M_V = 1$	1%

TABLE VI
PARAMETERS OF EXAMPLE COIL DESIGN IN TABLE V

Parameters	Values
L_1, L_2	175 μH, 175 μH
M	43 μH
f_0	88 kHz
C_1, C_2	19.2 nF, 19.2 nF
r_1 at 100 kHz, r_2 at 100 kHz	104 mΩ, 104 mΩ

The designed values of the example coils are listed in Table V. Loss factor $\lambda_{coil} = 1\%$ when $f_N = f_{NH}$, with $M_V = 1$, $k = 0.247$, $Z_N = 2.8$, and $Q = 1043$. Inductances and ESR, resonant frequency, and the resonant capacitances for the designed coils in Table V are listed in Table VI.

The designed coils are simulated with the circuit topology in Fig. 1(a), with $V_{in} = 400$ V and $I_{out} = 8.2$ A. The output voltage varies from 400 to 200 V. Fig. 10 shows the simulation waveforms when $V_{out} = 400$ V and $V_{out} = 200$ V using the parameters in Table VI. The switching frequency is 100 kHz when $V_{out} = 400$ V and is 107 kHz when $V_{out} = 200$ V. The procedure for the physical realization of coils designed for $f_N = 1$ is described in the Appendix.

Sometimes the aluminum plates are placed under the lower ferrite and above the higher ferrite in order to shield other elements of the system [22], [44]. The aluminum plates introduce extra shielding losses that will decrease the efficiency, so they should be optimized together with the windings and ferrite plates when added to the coils [45], [46]. This is not discussed in this paper.

V. EXPERIMENTAL VERIFICATION

A. Coils

Following the procedure in Table V, coils with 62 mm R_{inner}, 125 mm R_{outer}, and 20 turns of 1650/44 litz wire were selected and built as shown in Fig. 11. The 250 mm × 250 mm ferrite plate was composed of four pieces of 150 mm × 100 mm × 5 mm of EPCOS N95 ferrite. The gap between the coils was set as 100 mm. The measured parameters are listed in Table VII. All the values in Table VII were measured in the presence of both transmitter and receiver coils, as shown in Fig. 11(c), with a 100-mm air gap.

Fig. 12 shows the full-bridge inverter, rectifier, and bank of resonant capacitors to test the coils. The inverter was built with STY139N65M5 from STMicroelectronics. Fast recovery epi-

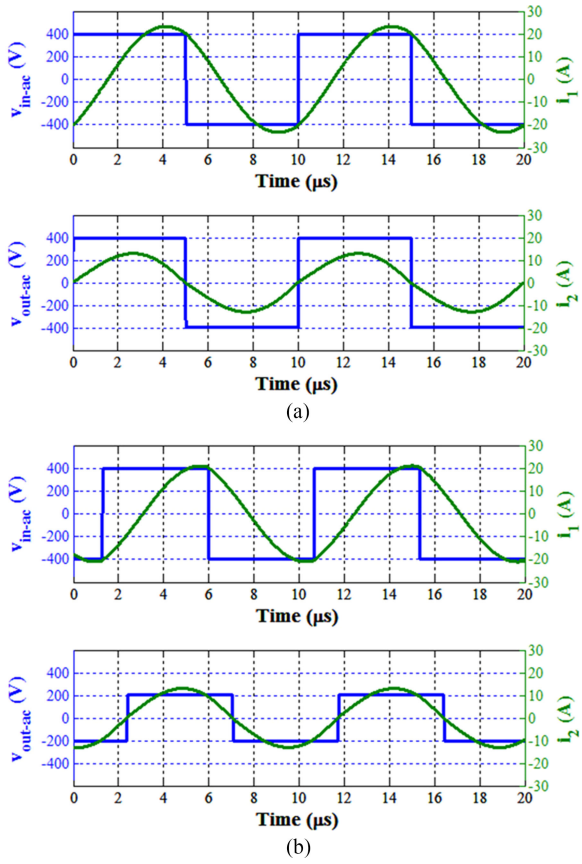

Fig. 10. Simulation waveforms of inverter output voltage $v_{\text{ac\_in}}$ and current i_1, rectifier input voltage $v_{\text{out\_ac}}$ and current i_2 for circuit topology in Fig. 1: (a) peak power with $V_{\text{in}} = 400$ V, $V_{\text{out}} = 400$ V, $I_{\text{out}} = 8.2$ A, and $f_s = 100$ kHz; (b) half power with $V_{\text{in}} = 400$ V, $V_{\text{out}} = 200$ V, $I_{\text{out}} = 8.2$ A, and $f_s = 107$ kHz. Parameters of the converter and coils are listed in Table VI.

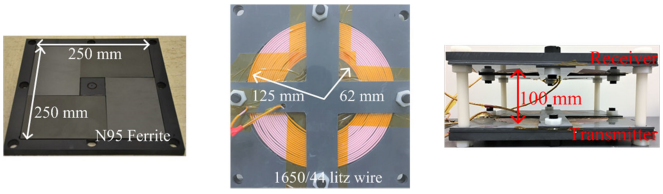

Fig. 11. Fabricated coils that were designed for 3.3 kW at $f_N = f_{\text{NH}}$ as in Table VI following the procedure in Table III and Table V with (a) four pieces of 150 mm × 100 mm × 5 mm of EPCOS N95 ferrite plates, (b) winding with 1650/44 litz wire, and (c) 100 mm air gap.

TABLE VII
SIMULATED AND MEASURED PARAMETERS OF COILS DESIGNED FOR $f_N = f_{\text{NH}}$ IN TABLE VI

Parameters	Simulated values	Measured values
L_1, L_2	175 μH, 175 μH	166 μH, 163 μH
M	43 μH	39 μH
k	0.247	0.25
r_1 at 100 kHz r_2 at 100 kHz	104 mΩ, 104 mΩ	110 mΩ, 108 mΩ

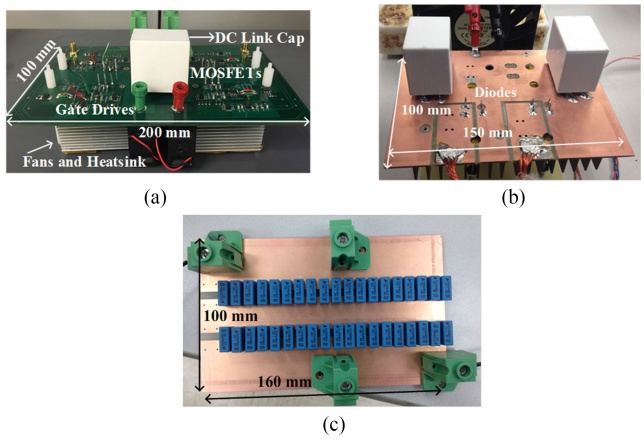

Fig. 12. (a) Full bridge inverter, (b) rectifier with diode bridges, and (c) resonant capacitor bank with 19.8 nF and 1.4 kV voltage rating to test the coils in Fig. 11.

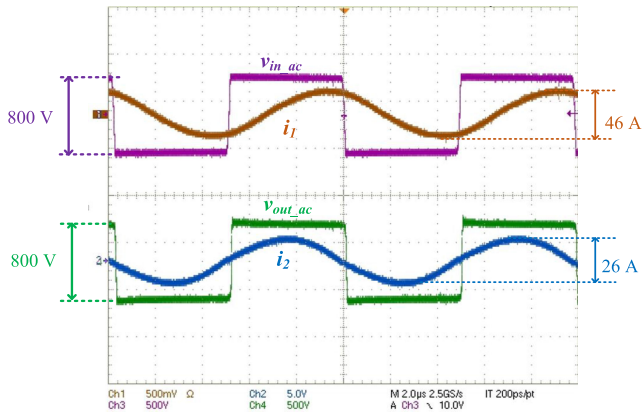

Fig. 13. Waveforms of inverter and rectifier for circuit topology in Fig. 1 when $V_{\text{in}} = 400$ V, $V_{\text{out}} = 400$ V, $I_{\text{out}} = 8.2$ A, and $f_s = 100$ kHz.

taxial diodes DSEI120-06A from IXYS were used for the rectifier. The resonant capacitance is 19.8 nF for C_1 and C_2.

B. Experimental Results

Fig. 13 shows the measured waveforms of inverter output voltage $v_{\text{in\_ac}}$ and current i_1, as well as rectifier input voltage $v_{\text{out\_ac}}$ and current i_2 at peak power. Voltage gain M_V is 1 when $V_{\text{in}} = 400$ V and $V_{\text{out}} = 400$ V. Voltages $v_{\text{in\_ac}}$ and $v_{\text{out\_ac}}$ were measured with the Tektronix THDP0200 voltage differential probes; current i_1 was measured with the PEM CWT015 Rogowski coil; and current i_2 was measured with the Tektronix A6302 current probe and Tektronix TM503B current probe amplifier. On the transmitter side, i_1 lags $v_{\text{in\_ac}}$ because the switching frequency is designed to be higher than the resonance frequency. Zero-voltage turn-on is realized for all the devices under all the load conditions, as illustrated in (29) and Fig. 4(b). The trade-off is the higher turn-off loss of the inverter devices and higher conduction loss due to circulating energy.

Switching frequency f_s was changed for different output voltages in the experiment without phase shift for the inverter output voltage. Fig. 14 shows f_s and λ_{coil} in experiment for different load conditions. The loss factor of the coils at peak power is

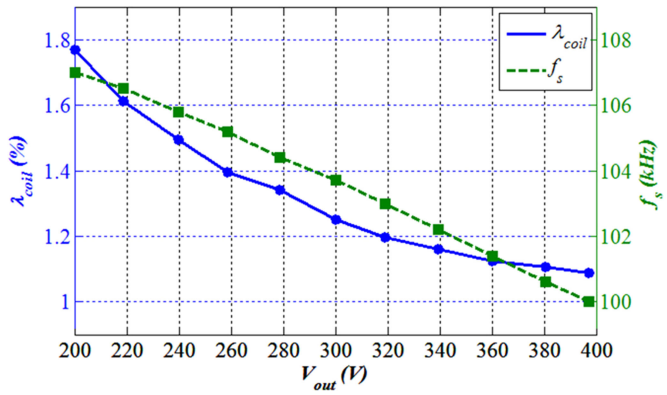

Fig. 14. Switching frequency and measured coils' efficiency with $I_{\rm out} = 8.2$ A, $V_{\rm out} = 200$ to 400 V, and the specifications in Table IV. The switching frequency was changed from 107 to 100 kHz for different voltage gains and constant output current.

1.1%. In Fig. 14, the coils' efficiency increases proportionately with the output voltage because the switching frequency is becoming closer to resonant frequency. Figs. 13 and 14 verify that the desired power transferability and loss factor, as well as zero-voltage turn-on of the inverter devices, are satisfied using the design method. The end-to-end efficiency of the circuit in Fig. 1(a) is 95.9% at peak power with the fabricated coils.

VI. Conclusion

In this paper, the coil parameters were designed sequentially to satisfy the requirements of power transferability and efficiency for series–series IPT system. The parameters were normalized as coupling coefficient *k*, normalized switching frequency f_N, normalized impedance Z_N, coil quality factor *Q*, and turns ratio *n*. The power transferability is determined by *n* when the geometries are the same for the transmitter and receiver coils. The efficiency requirement is satisfied by choosing $Z_N = Z_{\rm Nopt}$ and making $Q > Q_{Z\rm Nopt}$, where $Z_{\rm Nopt}$ is the optimal value of Z_N, and $Q_{Z\rm Nopt}$ is the *Q* value for the desired loss factor $\lambda_{\rm coil}$ when $Z_N = Z_{\rm Nopt}$. The physical realization for the designed electrical parameters was optimized by parametric sweep in finite-element simulation. The inner radii and outer radii of the winding, $R_{\rm inner}$ and $R_{\rm outer}$, as well as the size of litz wire, were selected for $Q > Q_{Z\rm Nopt}$. Number of turns *N* is chosen for $Z_N = Z_{\rm Nopt}$.

Following this procedure, a set of coils was designed for the operating condition when the compensation capacitor resonates with leakage inductance. In order to meet the efficiency specification when transferring 3.3-kW power across a 100-mm gap, the coils dimensions should be no smaller than 250 mm × 250 mm. Litz wire with strands of AWG 44 is selected for negligible skin effect, and either 1650 or 2625 strands should be chosen to guarantee high values of coil quality factor. The coils were built and tested in a series–series IPT system rated at 3.3 kW. Coils efficiency reached 98.9% at 100 kHz for peak power. The operating frequency should range between 100–107 kHz to realize requirements of power transferability. Soft-turn-ons were achieved for switches. Misalignment can be done for future research.

TABLE VIII
Sequential Design of Electrical Parameters for $f_N = 1$

Parameters	Method
n	(40)
$Z_N = Z_{\rm Nopt}$	(41)
$Q_{Z\rm Nopt}$ for $\lambda_{\rm coil}$	(37)

Appendix

When the switching frequency is equal to the resonant frequency, the compensation capacitor resonates with the self-inductance of the coils, and $f_N = 1$. The procedure of coil design for $f_N = 1$ is the same as $f_N = f_{\rm NH}$ but with different equations.

A. Sequential Design of Electrical Parameters for $f_N = 1$

When $f_N = 1$, M_V, $\lambda_{\rm coil}$, and $\varphi_{Z\rm in}$ in (24)–(26) are simplified as

$$M_V = 1/(k \cdot Z_N \cdot n) \tag{36}$$

$$\lambda_{\rm coil} = n \cdot \frac{Z_N}{Q} + \frac{Z_N}{k^2 \cdot Q} \cdot \left(\frac{1}{n \cdot Z_N} + \frac{1}{Q}\right)^2 \tag{37}$$

$$\varphi_{Z\rm in} = 0. \tag{38}$$

The optimal Z_N when the efficiency requirement is satisfied with smallest value of *Q* is derived by solving the equation when the derivative of (37) to Z_N is equal to zero. The expression is

$$Z_{N\rm opt} = 1\Big/\left(k \cdot n^{\frac{3}{2}}\right). \tag{39}$$

Voltage gain M_V when $Z_N = Z_{\rm Nopt}$ is derived by combining (36) and (39) as

$$M_V = \sqrt{n}. \tag{40}$$

Then $Z_{\rm Nopt}$ is represented with *k* and M_V by combining (39) and (40) as

$$Z_{N\rm opt} = 1\Big/\left(k \cdot M_V^3\right). \tag{41}$$

Equation (41) shows $Z_{\rm Nopt}$ is independent of *Q*. This means Z_N and *Q* can be optimized sequentially. The smallest value of *Q* when $Z_N = Z_{\rm Nopt}$, which is represented as $Q_{Z\rm Nopt}$, is calculated from (37) for required $\lambda_{\rm coil}$. Fig. 15 shows $Z_{\rm Nopt}$ and $Q_{Z\rm Nopt}$ versus M_V and *k*. Table VIII summarizes the sequential design of electrical parameters for $f_N = 1$.

B. Physical Realization of Electrical Parameters for $f_N = 1$

The physical parameters, including inner radii $R_{\rm inner}$, outer radii $R_{\rm outer}$, turns number *N*, and the size of litz wire, are selected sequentially to realize $Z_N = Z_{\rm Nopt}$ and $Q > Q_{Z\rm Nopt}$ when $f_N = 1$.

The values of $Z_{\rm Nopt}$ for different values of $R_{\rm outer}$ and $R_{\rm inner}$ are calculated from (41), with $M_V = 1$ and *k* in Fig. 7(a), as plotted in Fig. 16(a). The turns number *N* to realize $Z_N = Z_{\rm Nopt}$ is calculated from (34) and plotted in Fig. 16(b).

The values of $Q_{Z\rm Nopt}$ for $\lambda_{\rm coil} = 1\%$ is derived from (37) with $Z_N = Z_{\rm Nopt}$. The results of $Q_{Z\rm Nopt}$ are plotted for differ-

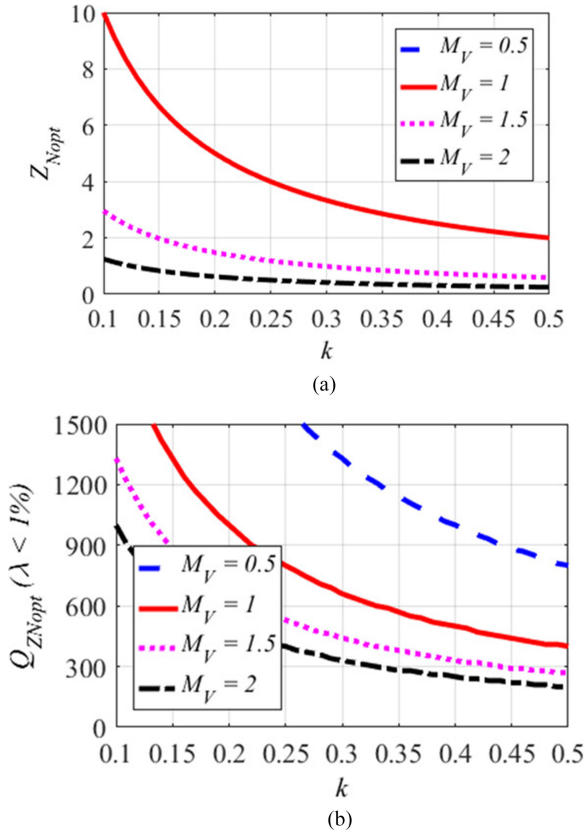

Fig. 15. (a) Z_{Nopt} in (41) and (b) $Q_{Z\mathrm{Nopt}}$ for $\lambda_{\mathrm{coil}} = 1\%$ versus M_V and k when $f_N = 1$.

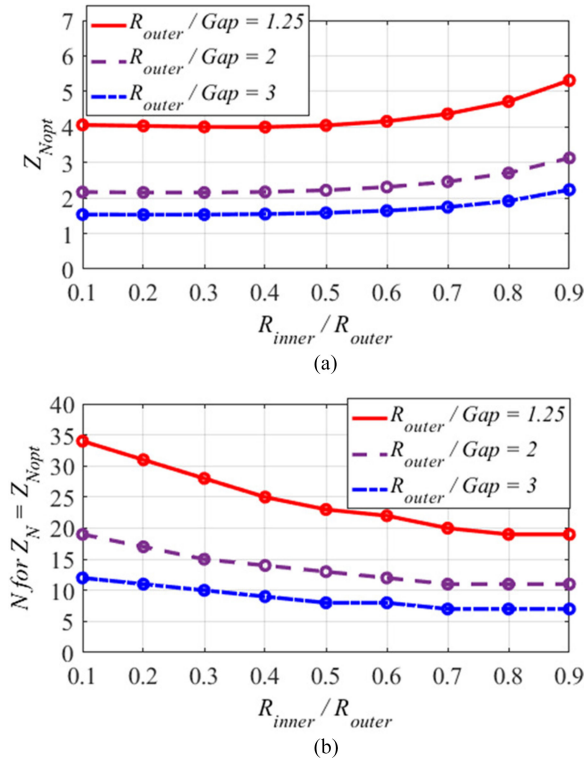

Fig. 16. Z_{Nopt} versus R_{inner} and R_{outer} with k in Fig. 7(a) and $M_V = 1$, calculated from (41). The gap is 100 mm as shown in Fig. 6 and Table IV, and R_{outer} is normalized to gap. The normalized $R_{\mathrm{outer}} = 1.25$, 2, and 3 represent $R_{\mathrm{outer}} = 125$, 250, and 300, respectively.

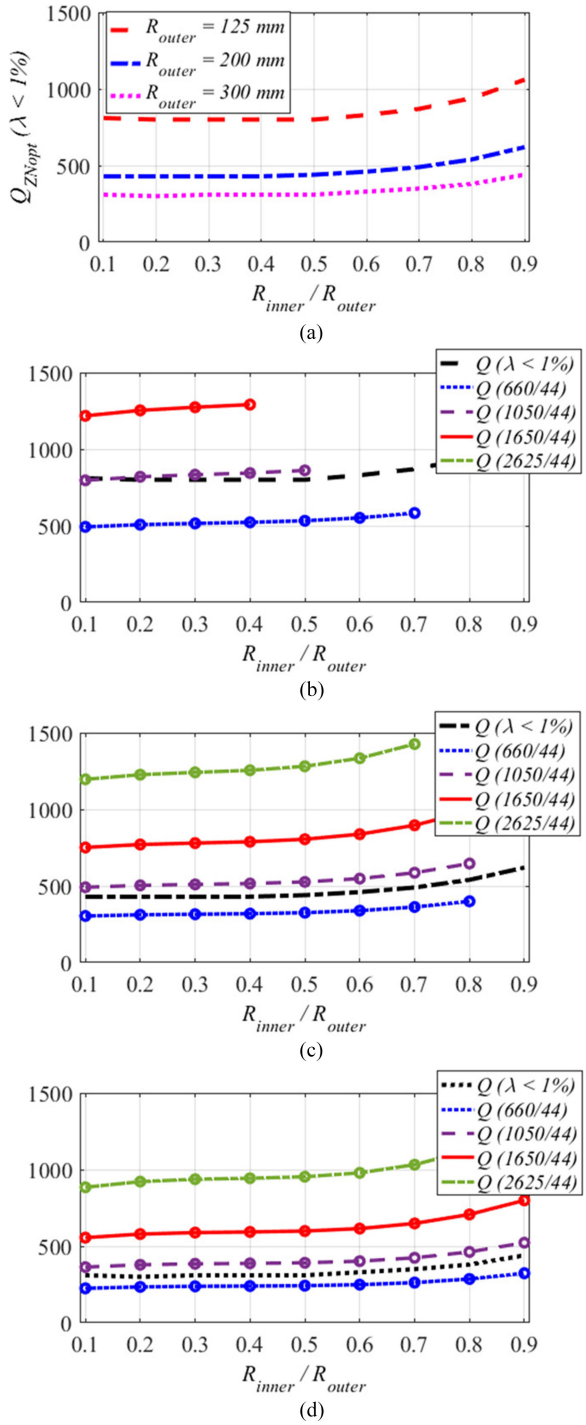

Fig. 17. When $f_N = 1$, (a) $Q_{Z\mathrm{Nopt}}$ is calculated from $\lambda_{\mathrm{coil}} = 1\%$ in(37) with $Z_N = Z_{\mathrm{Nopt}}$ in Fig. 16(a) and k in Fig. 7(a). The values of Q with different litz wires (660, 1050, 1650, 2625 strands of AWG #44 wire) and the number of turns N in Fig. 16(b) for R_{outer} of (b) 125, (b) 200, and (b) 300. The candidates of R_{inner} and R_{outer} to select is when $Q > Q_{\mathrm{Nopt}}$.

ent values of R_{outer} and R_{inner} in Fig. 17(a). The coil quality factors with four litz wires, 660, 1050, 1650, and 2625 strands of AWG #44 wires, are compared with $Q_{Z\mathrm{Nopt}}$ in Fig. 17(b)–(d), with R_{outer} to be 125, 200, and 300. The values of R_{outer}, R_{inner}, and the wire size that produce $Q > Q_{Z\mathrm{Nopt}}$ in Fig. 17(b)–(d) are the candidates that satisfy the requirements

TABLE IX
PROCEDURE OF PHYSICAL REALIZATION AND DESIGN RESULTS FOR $f_N = 1$

Parameters	Design methods	Values
R_{outer}	$Q > Q_{Z\text{Nopt}}$ in Fig. 17 ($Q = 861$)	125 mm
R_{inner}	$Q > Q_{Z\text{Nopt}}$ in Fig. 17	62.5 mm
Strands number	$Q > Q_{Z\text{Nopt}}$ in Fig. 17	1650
k	Fig. 7(a) at $R_{\text{inner}} = 62.5$ mm and $R_{\text{outer}} = 125$ mm	0.247
Z_{Nopt}	(41) with $k = 0.247$ and $M_V = 1$	4.0
N	(34) with $Z_{\text{Nopt}} = 4.0$ and L_0 in Fig. 7(b)	23
λ_{coil}	(37) with $Z_N = 4.0$, $Q = 861$, $k = 0.247$, $M_V = 1$	1%

TABLE X
PARAMETERS OF EXAMPLE COIL DESIGN IN TABLE IX

Parameters	Values
L_1, L_2	249 μH, 249 μH
M	62 μH
f_0	100 kHz
C_1, C_2	10.2 nF, 10.2 nF
r_1 at 100 kHz, r_2 at 100 kHz	182 mΩ, 182 mΩ

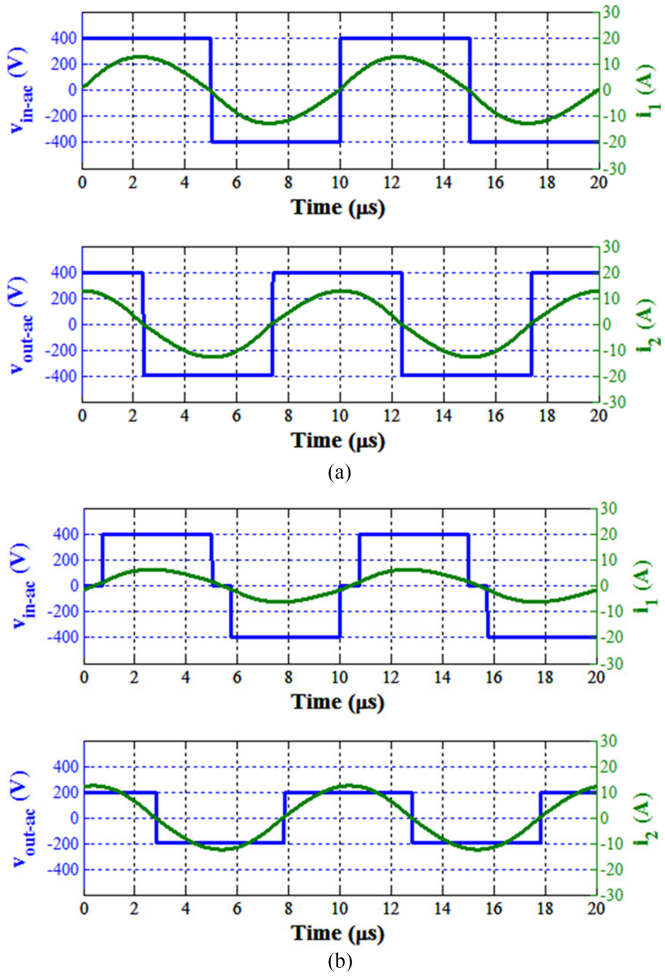

Fig. 18. Simulation waveforms of inverter output voltage $v_{\text{ac\_in}}$ and current i_1, rectifier input voltage $v_{\text{out\_ac}}$ and current i_2 for circuit topology in Fig. 1 when $f_N = 1$: (a) peak power with $V_{\text{in}} = 400$ V, $V_{\text{out}} = 400$ V, $I_{\text{out}} = 8.2$ A, and $f_s = 100$ kHz; (b) half power with $V_{\text{in}} = 400$ V, $V_{\text{out}} = 200$ V, $I_{\text{out}} = 8.2$ A, and $f_s = 100$ kHz. The parameters of converter and coils are listed in Table X.

of power transferability and efficiency. The corresponding turns number N is found in Fig. 16(b).

Table IX summarizes the procedure of physical realization when $f_N = 1$. The corresponding inductances and ESR, resonant frequency, and resonant capacitance are listed in Table X.

The designed coils are simulated with the circuit topology shown in Fig. 1(a), with $V_{\text{in}} = 400$ V and $I_{\text{out}} = 8.2$ A. The output voltage varies for different load conditions by phase-shifting the inverter voltage. Fig. 18 shows simulation waveforms with coils designed for $f_N = 1$ at peak power when the output voltage is 400 V, and at half power when the output voltage is 200 V. The switching frequency is fixed at 100 kHz for different load conditions.

REFERENCES

[1] S. Y. R. Hui, W. Zhong and C. K. Lee, "A critical review of recent progress in mid-range wireless power transfer," *IEEE Trans. Power Electron.*, vol. 29, no. 9, pp. 4500–4511, Sep. 2014.

[2] G. A. Covic and J. T. Boys, "Modern trends in inductive power transfer for transportation applications," *IEEE J. Emerg. Sel. Topics Power Electron.*, vol. 1, no. 1, pp. 28–41, Mar. 2013.

[3] U. K. Madawala and D. J. Thrimawithana, "A bidirectional inductive power interface for electric vehicles in V2G systems," *IEEE Trans. Ind. Electron.*, vol. 58, no. 10, pp. 4789–4796, Oct. 2011.

[4] S. Li and C. C. Mi, "Wireless power transfer for electric vehicle applications," *IEEE J. Emerg. Sel. Topics Power Electron.*, vol. 3, no. 1, pp. 4–17, Mar. 2015.

[5] S. Lukic and Z. Pantic, "Cutting the cord: Static and dynamic inductive wireless charging of electric vehicles," *IEEE Electrific. Mag.*, vol. 1, no. 1, pp. 57–64, Sep. 2013.

[6] L. Kibok, Z. Pantic, and S. M. Lukic, "Reflexive field containment in dynamic inductive power transfer systems," *IEEE Trans. Power Electron.*, vol. 29, no. 9, pp. 4592–4602, Sep. 2014.

[7] C.-S. Wang, O. H. Stielau, and G. A. Covic, "Design considerations for a contactless electric vehicle battery charger," *IEEE Trans. Ind. Electron.*, vol. 52, no. 5, pp. 1308–1314, Oct. 2005.

[8] C.-S. Wang, G. A. Covic, and O. H. Stielau, "Power transfer capability and bifurcation phenomena of loosely coupled inductive power transfer systems," *IEEE Trans. Ind. Electron.*, vol. 51, no. 1, pp. 148–157, Feb. 2004.

[9] J. L. Villa, J. Sallan, J. F. Sanz Osorio, and A. Llombart, "High-misalignment tolerant compensation topology for ICPT systems," *IEEE Trans. Ind. Electron.*, vol. 59, no. 2, pp. 945–951, Feb. 2012.

[10] Z. Pantic and S. M. Lukic, "Framework and topology for active tuning of parallel compensated receivers in power transfer systems," *IEEE Trans. Power Electron.*, vol. 27, no. 11, pp. 4503–4513, Nov. 2012.

[11] C. Y. Huang, J. T. Boys, and G. A. Covic, "LCL pickup circulating current controller for inductive power transfer systems," *IEEE Trans. Power Electron.*, vol. 28, no. 4, pp. 2081–2093, Apr. 2013.

[12] R. Bosshard, U. Badstübner, J. W. Kolar, and I. Stevanović, "Comparative evaluation of control methods for Inductive Power Transfer," in *Proc. Int. Conf. Renew. Energy Res. Appl.*, 2012, pp. 1–6.

[13] R. Chen *et al.*, "Analysis and parameters optimization of a contactless IPT system for EV charger," in *Proc. Appl. Power Electron. Conf.*, 2014, pp. 1654–1661.

[14] C. Zheng *et al.*, "High-efficiency contactless power transfer system for electric vehicle battery charging application," *IEEE J. Emerg. Sel. Topics Power Electron.*, vol. 3, no. 1, pp. 65–74, Mar. 2015.

[15] T. Diekhans and R. W. De Doncker, "A dual-side controlled inductive power transfer system optimized for large coupling factor variations and partial load," *IEEE Trans. Power Electron.*, vol. 30, no. 11, pp. 6320–6328, Nov. 2015.

[16] J. Deng, W. Li, T. D. Nguyen, S. Li, and C. C. Mi, "Compact and efficient bipolar coupler for wireless power chargers: Design and analysis," *IEEE Trans. Power Electron.*, vol. 30, no. 11, pp. 6130–6140, Nov. 2015.

[17] M. Budhia, J. T. Boys, G. A. Covic, and C. Y. Huang, "Development of a single-sided flux magnetic coupler for electric vehicle IPT charging systems," *IEEE Trans. Ind. Electron.*, vol. 60, no. 1, pp. 318–328, Jan. 2013.

[18] S. Raabe and G. A. Covic, "Practical design considerations for contactless power transfer quadrature pick-ups," *IEEE Trans. Ind. Electron.*, vol. 60, no. 1, pp. 400–409, Jan. 2013.
[19] M. Lu and K. D. T. Ngo, "Sequential design for coils in series-series inductive power transfer using normalized parameters," in *Proc. IEEE PELS Workshop Emerg. Technol.: Wireless Power*, 2016, pp. 1–6.
[20] R. Bosshard, J. Mühlethaler, J. W. Kolar, and I. Stevanović, "Optimized magnetic design for inductive power transfer coils," in *Proc. Appl. Power Electron. Conf.*, 2013, pp. 1812–1819.
[21] O. H. Stielau and G. A. Covic, "Design of loosely coupled inductive power transfer systems," in *Proc. Int. Conf. Power Syst. Technol.*, 2000, pp. 85–90.
[22] M. Budhia, G. A. Covic, and J. T. Boys, "Design and optimization of circular magnetic structures for lumped inductive power transfer systems," *IEEE Trans. Power Electron.*, vol. 26, no. 11, pp. 3096–3108, Nov. 2011.
[23] J. Sallan, J. L. Villa, A. Llombart, and J. F. Sanz, "Optimal design of ICPT systems applied to electric vehicle battery charge," *IEEE Trans. Ind. Electron.*, vol. 56, no. 6, pp. 2140–2149, Jun. 2009.
[24] E. Waffenschmidt and T. Staring, "Limitation of inductive power transfer for consumer applications," in *Proc. Eur. Conf. Power Electron. Appl.*, 2009, pp. 1–10.
[25] O. Knecht, R. Bosshard, and J. W. Kolar, "High-efficiency transcutaneous energy transfer for implantable mechanical heart support systems," *IEEE Trans. Power Electron.*, vol. 30, no. 11, pp. 6221–6236, Nov. 2015.
[26] R. Bosshard, J. W. Kolar, J. Muhlethaler, I. Stevanovic, B. Wunsch, and F. Canales, "Modeling and η-α-Pareto optimization of inductive power transfer coils for electric vehicles," *IEEE J. Emerg. Sel. Topics Power Electron.*, vol. 3, pp. 50–64, 2015.
[27] Q. Li and Y. C. Liang, "An inductive power transfer system with a high-Q resonant tank for mobile device charging," *IEEE Trans. Power Electron.*, vol. 30, no. 11, pp. 6203–6212, Nov. 2015.
[28] F. Y. Lin, G. A. Covic, and J. T. Boys, "Evaluation of magnetic pad sizes and topologies for electric vehicle charging," *IEEE Trans. Power Electron.*, vol. 30, no. 11, pp. 6391–6407, Nov. 2015.
[29] C. Zheng, H. Ma, J. S. Lai, and L. Zhang, "Design considerations to reduce gap variation and misalignment effects for the inductive power transfer system," *IEEE Trans. Power Electron.*, vol. 30, no. 11, pp. 6108–6119, Nov. 2015.
[30] S. Raju, R. Wu, M. Chan, and C. P. Yue, "Modeling of mutual coupling between planar inductors in wireless power applications," *IEEE Trans. Power Electron.*, vol. 29, no. 1, pp. 481–490, Jan. 2014.
[31] W. G. Hurley and M. C. Duffy, "Calculation of self and mutual impedances in planar magnetic structures," *IEEE Trans. Magn.*, vol. 31, no. 4, pp. 2416–2422, Jul. 1995.
[32] W. G. Hurley and M. C. Duffy, "Calculation of self- and mutual impedances in planar sandwich inductors," *IEEE Trans. Magn.*, vol. 33, no. 3, pp. 2282–2290, May 1997.
[33] Y. P. Su, X. Liu, and S. Y. Hui, "Extended theory on the inductance calculation of planar spiral windings including the effect of double-layer electromagnetic shield," *IEEE Trans. Power Electron.*, vol. 23, no. 4, pp. 2052–2061, Jul. 2008.
[34] Y. P. Su, X. Liu, and S. Y. R. Hui, "Mutual inductance calculation of movable planar coils on parallel surfaces," *IEEE Trans. Power Electron.*, vol. 24, no. 4, pp. 1115–1123, Apr. 2009.
[35] C. R. Sullivan, "Optimal choice for number of strands in a litz-wire transformer winding," *IEEE Trans. Power Electron.*, vol. 14, no. 2, pp. 283–291, Mar 1999.
[36] C. R. Sullivan, "Computationally efficient winding loss calculation with multiple windings, arbitrary waveforms, and two-dimensional or three-dimensional field geometry," *IEEE Trans. Power Electron.*, vol. 16, no. 1, pp. 142–150, 2001.
[37] I. Lope, J. Acero, C. Carretero, I. Lope, J. Acero, and C. Carretero, "Analysis and optimization of the efficiency of induction heating applications with litz-wire planar and solenoidal coils," *IEEE Trans. Power Electron.*, vol. 31, no. 7, pp. 5089–5101, Jul. 2016.
[38] W. Zhang, S. C. Wong, C. K. Tse, and Q. Chen, "Design for efficiency optimization and voltage controllability of series–series compensated inductive power transfer systems," *IEEE Trans. Power Electron.*, vol. 29, no. 1, pp. 191–200, Jan. 2014.
[39] W. Zhang, S. C. Wong, C. K. Tse, and Q. Chen, "Analysis and comparison of secondary series- and parallel-compensated inductive power transfer systems operating for optimal efficiency and load-independent voltage-transfer ratio," *IEEE Trans. Power Electron.*, vol. 29, no. 6, pp. 2979–2990, Jun. 2014.
[40] Y. Zhang, T. Lu, Z. Zhao, F. He, K. Chen, and L. Yuan, "Selective wireless power transfer to multiple loads using receivers of different resonant frequencies," *IEEE Trans. Power Electron.*, vol. 30, no. 11, pp. 6001–6005, Nov. 2015.
[41] Ansys. User's Guide-Maxwell 3-D, Rev 6.0. Mar 2012. [Online] Available: www.ansys.com
[42] W. Zhang, J. C. White, A. M. Abraham, and C. C. Mi, "Loosely coupled transformer structure and interoperability study for EV wireless charging systems," *IEEE Trans. Power Electron.*, vol. 30, no. 11, pp. 6356–6367, Nov. 2015.
[43] R. Bosshard, U. Iruretagoyena, and J. W. Kolar, "Comprehensive evaluation of rectangular and double-D coil geometry for 50 kW/85 kHz IPT system," *IEEE J. Emerg. Sel. Top. Power Electron.*, vol. 4, no. 4, pp. 1406–1415, Dec. 2016.
[44] J. Kim *et al.*, "Coil design and shielding methods for a magnetic resonant wireless power transfer system," *Proc. IEEE*, vol. 101, no. 6, pp. 1332–1342, Jun. 2013.
[45] M. Lu and K. D. T. Ngo, "Pareto fronts for coils' efficiency versus stray magnetic field in inductive power transfer," in *Proc. IEEE PELS Workshop Emerg. Technol., Wireless Power*, 2016, pp. 1–5.
[46] M. Lu and K. D. T. Ngo, "Comparison of passive shields for coils in inductive power transfer," 2017 IEEE Applied Power Electronics Conference and Exposition (APEC), Tampa, FL, USA, 2017, pp. 1419–1424.

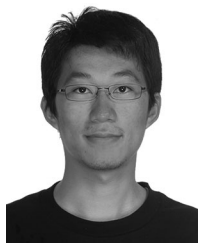

Ming Lu (S'16) was born in Shandong, China, in 1986. He received the B.S. and M.S. degrees in electrical engineering from Shanghai Jiao Tong University, Shanghai, China, in 2008 and 2012, respectively. He is currently working toward the Ph.D. degree in Electrical Engineering at the Center for Power Electronics Systems, Virginia Polytechnic Institute and State University, Blacksburg, VA, USA.

His current research interests include wireless power transfer for electric vehicles and wide bandgap power semiconductor devices.

Khai D. T. Ngo (S'82–M'84–SM'02–F'15) received the B.S. degree from California State Polytechnic University, Pomona, CA, USA, in 1979, and the M.S. and Ph.D. degrees from the California Institute of Technology, Pasadena, CA, USA, in 1980 and 1984, respectively, all in electrical and electronics engineering.

He is currently a Professor of electrical and computer engineering at Virginia Tech¸ Blacksburg, VA, USA. He was a Member of Technical Staff at General Electric Corporate Research and Development Center, Schenectady, NY, USA, from 1984 to 1988. Between 1988 and 2006, he was with the University of Florida, Gainesville, FL, USA. At Virginia Tech, he pursues technologies for integration and packaging of power passive and active components to realize building blocks for power electronic systems. These technologies lead to power conversion systems with higher efficiency and higher power density. He also focuses on topologies, control, emission, and integration issues for RF power converters. Other research interests include magnetic materials and components, energy reclamation, and power-integrated circuits.